Stress and Damage Mitigation from Oriented Nanostructures within the Radular Teeth of *Cryptochiton stelleri*

*Lessa Kay Grunenfelder, Enrique Escobar de Obaldia, Qianqian Wang, Dongsheng Li, Brian Weden, Christopher Salinas, Richard Wuhrer, Pablo Zavattieri, and David Kisailus**

Chiton are marine mollusks who use heavily mineralized and ultrahard teeth to feed on epilithic and endolithic algae on intertidal rocks. To fulfill this function, chiton teeth must be tough and wear-resistant. Impressive mechanical properties are achieved in the chiton tooth through a hierarchically arranged composite structure consisting of a hard shell of organic-encased and highly oriented nanostructured magnetite rods that surround a soft core of organic-rich iron phosphate. Microscopic and spectroscopic analyses combined with finite element simulations are used to probe the ultrastructural features and uncover structure–mechanical property relationships in the fully mineralized teeth of the gumboot chiton *Cryptochiton stelleri*. By understanding the effects of the nanostructured architecture within the chiton tooth, abrasion-resistant materials can be developed for tooling and machining applications, as well as coatings for equipment and medical implants.

1. Introduction

The development of wear resistant tooling and coatings is a difficult task, as wear resistance is not a material property, but rather dependent on a number of factors (e.g., hardness, microstructure, chemical composition, geometry, loading conditions, environment, etc.), requiring a multidisciplinary approach.[1–3] Hard ceramics and ceramic-based composites are commonly used in abrasive loading applications. However, these materials are problematic from an engineering perspective, as they are prone to brittle failure[4] and typically require processing at high temperatures and pressures, making microstructural control difficult. Cues for the design of abrasion resistance materials, however, are readily accessible in the form of biological systems, eliminating the need for a trial and error approach.

Biomineralizing organisms have evolved to form complex, hierarchical structures that are adapted to mitigate predation and environmental stresses. These biological composites, through the addition of small quantities of organic, precisely control architectures from the nano- to macro-scale, and utilize organic-mineral interfaces to achieve remarkable material properties.[5–7] Adaptations in biological composites have led to enhancements in toughness, strength and abrasion-resistance over their constituent components, yielding properties rivaling those of modern engineering materials.[5,6,8] One such example is found in the feeding apparatus (radula) of the chiton, a marine snail that produces one of the most abrasion-resistant structures in the animal kingdom.[9,10] The chiton exhibits selective biomineralization, with shell plates consisting of aragonitic $CaCO_3$[11,12] and radular teeth mineralized by iron oxides and iron phosphates.[13–15]

The teeth of chitons are arranged in parallel rows on a tongue-like feeding organ called a radula.[8,14] The radula of *Cryptochiton stelleri*, the largest species of chiton (**Figure 1**A), contains more than 70 rows of tricuspid teeth affixed to an organic membrane. The chiton uses these radular teeth to scrape algae from rocks (Figure 1B). The radula displays active mineralization, with the degree of mineralization increasing from a completely non-mineralized structure consisting of alpha-chitin at the posterior end to a fully mineralized tooth at the anterior end (Figure 1C). This mineralization process was shown to be guided by organic fibers within the tooth.[8] The chiton tooth is a complex hierarchically-arranged biological composite, with an elegant design spanning multiple length scales. At the macroscale, the teeth of *C. stelleri* consist of tricuspid curved structures (Figure 1D). The rasping process of the chiton has led to the designation of the concavely bent front side as the leading edge of the tooth, and the convexly bent opposing side as the trailing edge.[16] The repeated cyclic mechanical loading of chiton teeth during rasping necessitates that they are both wear and abrasion resistant.[10] Thus, the teeth of *C. stelleri* are mineralized with a shell of magnetite,[6,8,11] displaying the highest hardness of any reported biomineral,[6] surrounding a softer core of hydrated iron phosphate.[4,5,11,14] Initial analysis of the magnetite shell revealed rod-like elements consisting of randomly oriented crystallites,

Dr. L. K. Grunenfelder, Dr. Q. Wang, Dr. D. Li, B. Weden, C. Salinas, Prof. D. Kisailus
Department of Chemical and Environmental Engineering
Bourns Hall B357, Riverside, CA 92521, USA
E-mail: david@engr.ucr.edu
E. E. de Obaldia, Prof. P. Zavattieri
School of Civil Engineering
Purdue University
West Lafayette, IN 47907, USA
Dr. R. Wuhrer
Advanced Materials Characterization Facility
University of Western Sydney
Penrith, NSW 2751, Australia

DOI: 10.1002/adfm.201401091

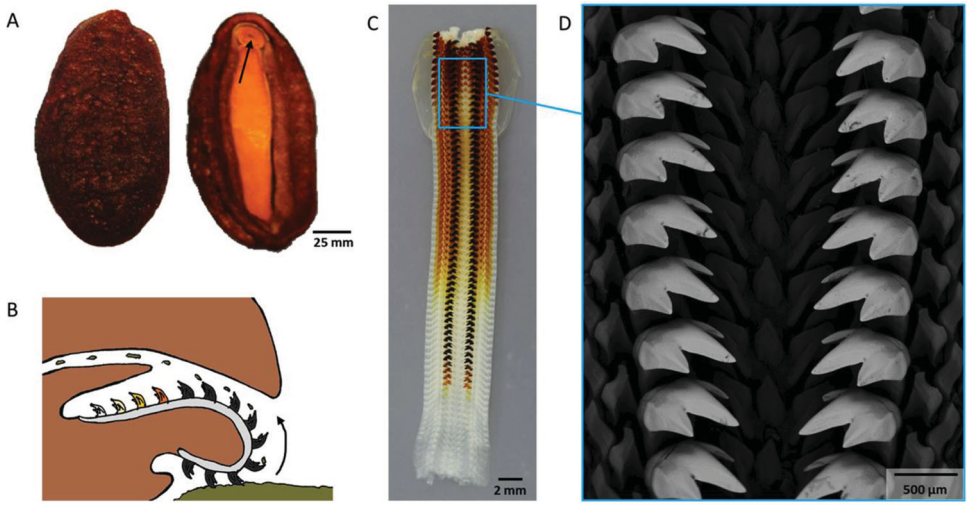

Figure 1. Chiton and its radular teeth. A) Overview of *Cryptochiton stelleri*, with the mouth shown by a black arrow; B) Schematic of rasping motion of chiton teeth during feeding; C) Dissected radula, with fully mineralized teeth at the top; D) Back-scatter SEM image showing the arrangement of teeth, as well as the contrast between the magnetite mineralized teeth and the organic radular membrane.

which influence the fracture toughness and wear resistance of the tooth.[5,16] The bulk structure, consisting of a hard shell with a soft core, is suggested to provide shock resistance and crack deflection in the tooth.[6,15] Clear corollaries can be drawn between the chiton radular teeth and mammalian teeth. Both biological systems display a hierarchical structure, employing a hard shell-soft core design, and contain rod-like architectures, which result in resistance to fatigue loading and deformation as a result of repetitive wear.[17–19] The chiton tooth is unique, however, in mineral composition and nano and microscale architecture. Here, we report toughening mechanisms observed in this biological composite at various length scales, revealing potential design strategies for next generation abrasion resistant materials.

2. Results

2.1. Core–Shell Architecture and Rod-Like Microstructure

To assess the effects of nano- and microstructural features of both local and global properties of functional radular teeth, fractured specimens from fully mineralized teeth were prepared. Analysis of a longitudinally fractured surface within the interior of the middle cusp of the tooth reveals a core–shell structure (**Figure 2**A). A closer observation of the leading edge of the shell region uncovered ≈200 nm diameter nanorods which are aligned parallel to the long axis of the tooth (Figure 2B). In contrast, the core region does not appear to have any specific orientation (Figure 2C). Examination of the fracture at the apex of the middle cusp (Figure 2D) demonstrates that nanorods extend parallel to the surface of the tooth, effectively wrapping the entire shell structure.

A latitudinal fracture close to the tip of the middle cusp of the tooth (Figure 2E,F) demonstrates that the nanorods follow the contour of the tooth, aligning parallel to its surface (highlighted with the yellow dashed lines in Figure 2A,D,F). This alignment of nearly hexagonally close-packed nanorods can clearly be observed in a latitudinal section near the leading edge of the tooth (Figure 2G). In addition, the fractured surfaces of these rods (Figure 2G) appear conchoidal. This can be explained through examination of the tooth mineralization process. An SEM image of a partially mineralized tooth (Figure 2H) shows the formation of large crystallites guided by organic fibers.[8] The cores of these crystallites are single crystalline and multifaceted in nature. Examination of fractured rods show features matching this morphology, with rods exhibiting smooth, and occasionally bipyramidal faceted fractures (circle in Figure 2G).

2.2. Micromechanical Analysis

High-resolution nanoindentation was performed to ascertain the regional hardness and modulus of the chiton tooth. Indents were performed on both latitudinal (**Figure 3**A–C) and longitudinal (Figure 3D–F) polished sections through the middle cusp of the tooth. The analysis plane was chosen such that the core of the tooth was exposed, to reveal the mechanical properties of the leading and trailing edges of the magnetite shell, as well as those of the iron phosphate core.

Modulus (Figure 3B,E) and hardness (Figure 3C,F) maps of latitudinal and longitudinal sections of the tooth reveal that the stiffest and hardest portion of the tooth is at the mid-point of the leading edge. In this region, the highest reported values of modulus and hardness were obtained (E = 130.8 ± 7.3 GPa and H = 10.2 ± 1.3 GPa in the latitudinal section, and E = 128.5 ± 5.0 GPa and H = 10.4 ± 0.8 GPa in the longitudinal section). Average values for modulus and hardness on the trailing edge were E = 114.8 ± 8.2 GPa and H = 8.2 ± 1.0 GPa in the latitudinal section, and E = 97.6 ± 11.3 GPa and H = 7.5 ± 1.4 GPa in the longitudinal section. The core region shows a notable reduction in modulus and hardness (E = 28.6 ± 7.7 GPa and H = 1.5 ± 0.8 GPa in the latitudinal section, and E = 29.4 ± 9.1 GPa and H = 1.6 ± 0.5 GPa in the longitudinal section). In

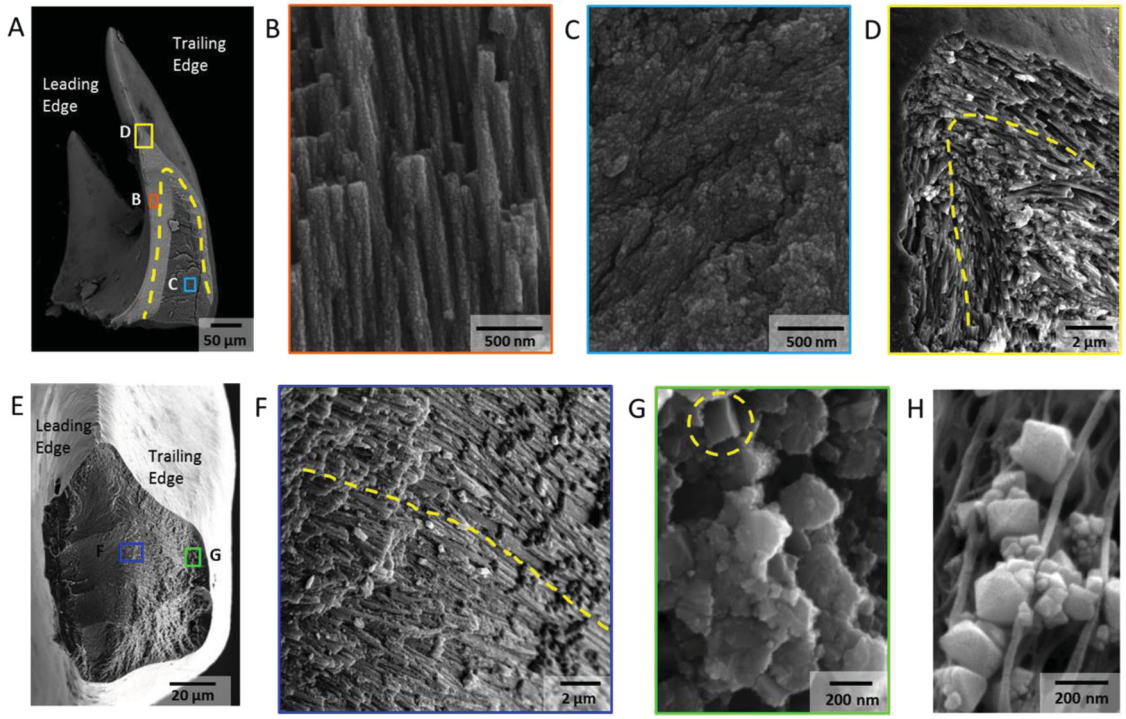

Figure 2. Core–shell architecture and local microstructural features of mineralized teeth. A) BSE microscopy overview of a longitudinal fracture, highlighting a heavily mineralized outer shell and organic rich core; B) Aligned and staggered nanorods in the leading edge of the shell; C) Amorphous core region; D) Apex of longitudinal fracture, revealing nanorod orientation and continuity around the shell of the tooth; E) Latitudinal fracture near the tip of the tooth; F) Center of the latitudinal fracture, demonstrating curvature of nanorods following the contour of the tooth; G) Latitudinal fracture within the shell region, highlighting highly oriented nature of nanorods; H) Micrograph of partially mineralized tooth showing mineral formation along alpha-chitin fibrils.

both latitudinal and longitudinal sections, there is a decrease in the modulus and hardness of the shell moving from the edges toward the core region (see Figure S1, Supporting Information).

On the leading edge of the longitudinal sample, a thin region with a reduced hardness and modulus is observed at the outermost edge. This reduction in mechanical properties is attributed to a crack through the tooth running parallel to the leading edge in the longitudinal section (Figure 3G). This crack traverses the entire leading edge, and is located 4.4 ± 2.0 µm into the tooth. Cracking was also observed between the hard shell of the tooth and the soft core (Figure 3H), with BSE microscopy revealing that some of the magnetite shell remains attached to the core material following fracture.

2.3. Surface Analysis

During rasping events, the surfaces of the radular teeth are placed in contact with rocky substrates. Thus, to interpret the role of microstructures within these surfaces, examination of longitudinally fractured fully mineralized teeth was performed. Upon close observation of the leading edge (**Figure 4**A), several interesting features are revealed. The outermost ≈2 µm of the tooth consists of a dense packing of sub-100 nm particles. This dense nanoparticulate region transitions to nanorods, which abruptly (within 1 µm) undergo a 90° rotation that aligns them with the long axis of the tooth. Examination of the trailing edge of the tooth (Figure 4B) reveals a thinner (approximately 1 µm) dense nanoparticulate layer that abruptly transitions to nanorods, which are oriented parallel to the tooth surface. Unlike the leading edge, no rotation of nanorods is observed on the trailing edge. The sizes of the rods at the leading and trailing edges were determined through image analysis of SEM images. Rods at the leading edge measured 193 ± 23 nm in diameter (Figure 4C), while rods at the trailing edge measured 250 ± 27 nm (Figure 4D).

2.4. Transmission Electron Microscopy of Tooth Surface

To uncover higher resolution ultrastructural features at the surface of the leading and trailing edges of the tooth, thin sections (see yellow lines in the inset micrographs in **Figures 5**A and E) were produced by focused ion beam lithography (FIB) and imaged using transmission electron microscopy (TEM). The orientation of the thin sections in both leading and trailing edges were selected to be perpendicular to the long axis of the tooth. TEM analysis at the leading edge of the tooth (Figure 5A) reveals the multiregional structure observed in SEM (Figure 4A). At the outermost edge of the tooth are closely packed nanoparticles (represented by green dots in Figure 5A). These nanoparticles (Figure 5B) have a wide size distribution, with diameters ranging from 8–60 nm, and generally increasing in size moving inward from the surface of

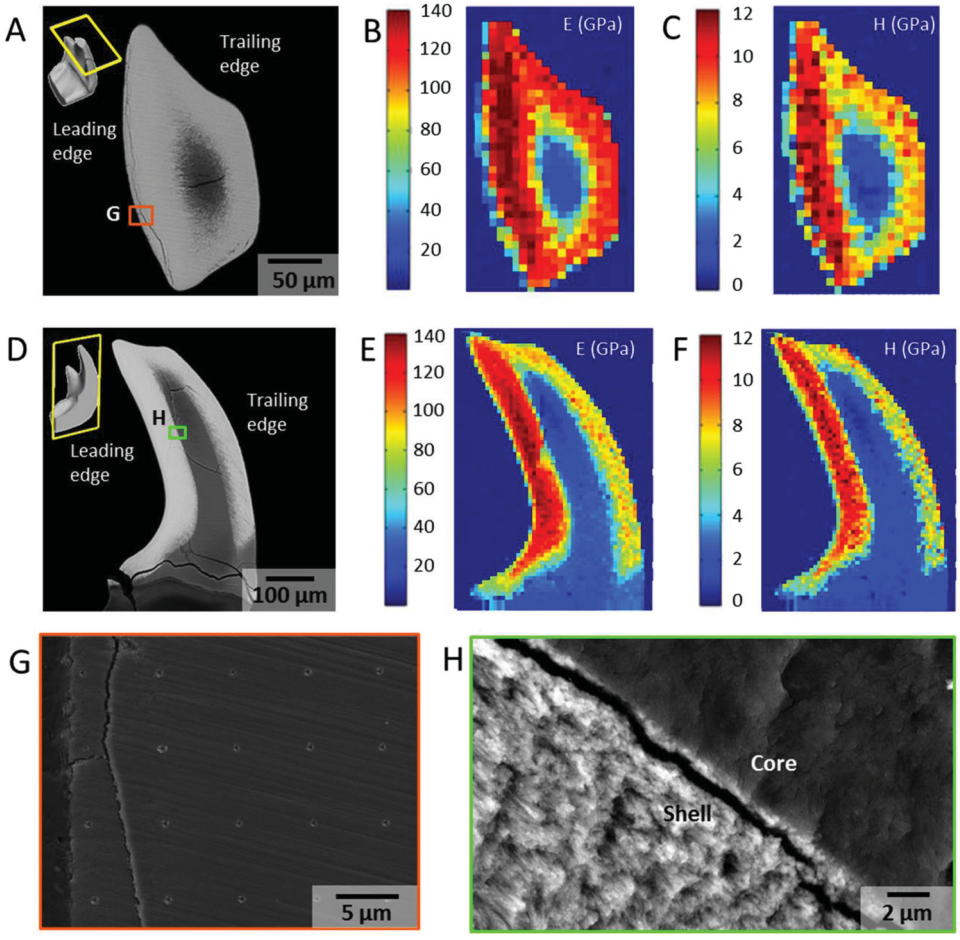

Figure 3. Nanomechanics of core and shell regions of a fully mineralized tooth in latitudinal and longitudinal sections. A) BSE micrograph of a latitudinal polished section showing the core–shell structure of the tooth; B) Modulus and C) Hardness maps from nanoindentation of a latitudinal section; D) BSE micrograph of a longitudinal polished section of the entire tooth, highlighting the thickness of leading and trailing edges as well as extent of core region throughout tooth; E) Modulus and F) Hardness maps from nanoindentation of the longitudinal section, demonstrating a clear interface between core and shell as well as a gradient from leading edge to trailing edge of the tooth; G) SEM image of the leading edge of the longitudinal section after indentation, highlighting a crack running parallel to the edge of the sample; H) BSE micrograph revealing cracking at the core–shell interface of the tooth.

the tooth. Selected area diffraction (Figure 5B, inset) confirms that the particles are magnetite crystallites with no preferred orientation. The nanoparticulate region transitions to rod-like structures (the long axis of these rods is highlighted by blue dashed lines in Figure 5A). TEM investigations of partially mineralized teeth have revealed an anisotropic arrangement of densely spaced organic fibers in the particulate region, a stark contrast to the aligned fibers which template nanorod formation in the bulk of the tooth (see Figure S2, Supporting Information). Closer analysis of the long axis of the rods at the leading edge (Figure 5C) not only confirms that the rods are oriented perpendicular to the tooth surface, but highlights their rough surface texture (also observed in SEM), and thin regions of organic between rods. Moving toward the interior of the tooth, these rod-like structures rotate 90° such that they are out of the plane of the micrograph/parallel to the surface of the tooth (represented by orange dashed circles in Figure 5A and at higher resolution in Figure 5D). In addition to the surface roughness and enveloping organic phase (Figure 5D), mineral bridges can be observed connecting adjacent rods (Figure 5D, inset).

TEM analysis of the trailing edge of the tooth reveals two regions, confirming SEM observations (Figure 4B). The outermost surface of the trailing edge, like the leading edge, consists of densely packed magnetite particles, which abruptly transition to nanorods that are parallel to the surface of the tooth (Figure 5E). No rod rotation is observed on the trailing edge. Higher resolution TEM shows that the nanoparticles (Figure 5F) and nanorods (Figure 5G) are less clearly defined. However, mineral bridges are once again observed, connecting adjacent nanorods. The striations running from left to right in Figure 5A,G are artifacts from the FIB process.

2.5. Quantitative Energy Dispersive Spectroscopy

Quantitative elemental analysis of the chiton tooth was performed using energy dispersive spectroscopy (EDS).

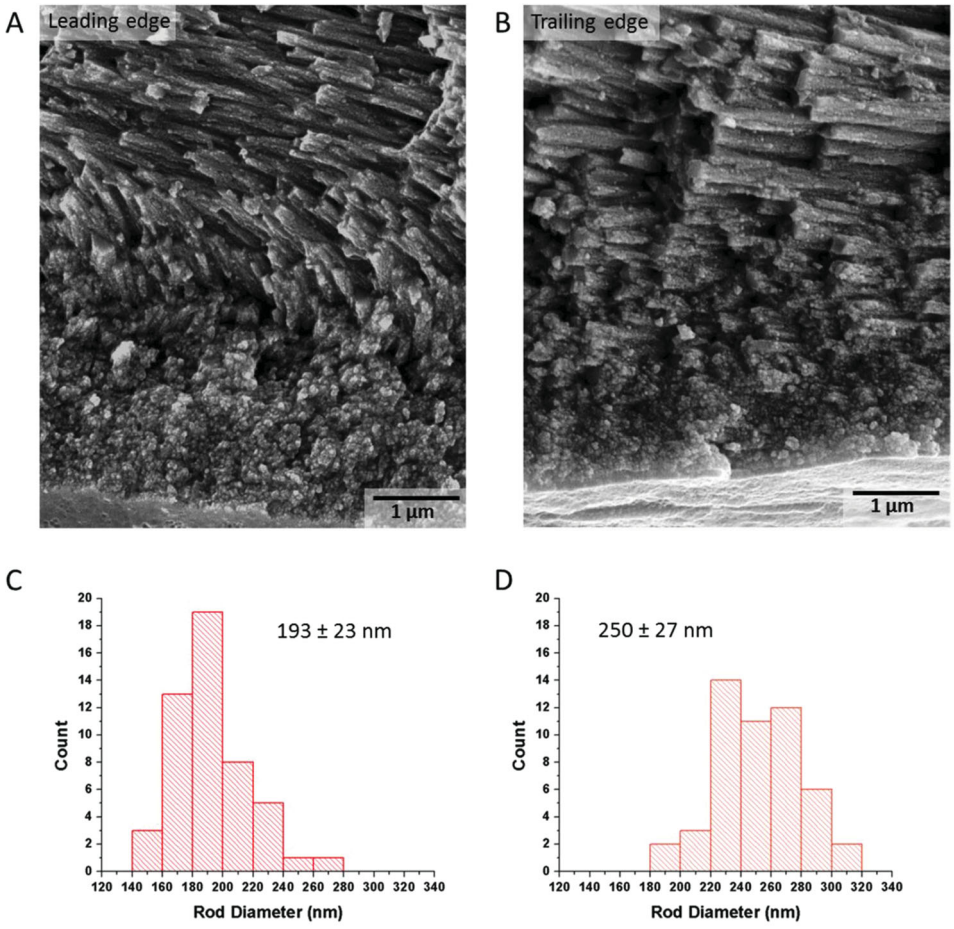

Figure 4. Surface analysis of the leading and trailing edges of the fully mineralized tooth. Longitudinal fracture surface of A) the leading edge, highlighting a 2 µm thick dense nanoparticulate layer, transitioning to nanorods (observed perpendicular to the field of view), which rotate 90° over a region of ≈1 µm to orient parallel to the tooth surface; Longitudinal fracture surface of B) the trailing edge, revealing a 1 µm thick dense nanoparticulate layer that abruptly transitions to nanorods oriented parallel to the tooth surface (no rod rotation observed); C) Histogram of rod diameters on the leading edge; D) Histogram of rod diameters on the trailing edge.

Quantitative X-ray maps (QXRM) were generated from collected X-ray maps (XRM). A false colored map of iron (blue) and phosphorus (green) distribution in a longitudinally polished section is presented in **Figure 6**A. This false colored map reveals that the magnetite shell at the leading edge of the tooth is thicker than at the trailing edge. This is confirmed in elemental line scans of Fe and P across the tooth (Figure 6B). Interestingly, there is an abrupt transition at the interface between the shell and core on the leading edge, contrasted with a gradual elemental change at the interface on the trailing edge of the tooth. The iron oxide (Fe_3O_4) content was measured in regions of the shell on both the leading and trailing edges (Figure 6C). This analysis reveals the magnetite content in the middle of the leading edge is 97.7 ± 0.9 wt%, exceeding the content on the trailing edge (ca. 95.8 ± 1.2 wt%).

Scatter diagrams, also known as scatter plots (Figure 6D), were generated from the X-ray maps by plotting pixel frequency versus element concentration profiles for two elements, Fe and P, against one another. A two-dimensional scatter diagram is a plot of the frequency of occurrence of intensity values for one element against another for each pixel in the X-ray map. The correlation of the points in the scatter diagram creates clusters, also referred to as nodes. The clusters represent distinct separated positions on the correlation diagram, which represent unique compositions that can be locally identified.[20,21] Various regions in the scatter plots, marked by colored boxes in Figure 6D, were selected. The regions of the sample corresponding to each composition are shown in a false-color map. This map reveals that the leading edge of the tooth is iron rich (red). A composition of lower iron concentration is observed on the trailing edge, and in a thin interfacial region between the shell and the core of the tooth on the leading edge (green). A thicker interfacial region, with greater phosphorus content, is observed on the trailing edge (purple). These interfacial regions are consistent with EDS line scan data (Figure 6B), showing a sharp transition between elements on the leading edge, and a gradual change on the trailing edge. Through selecting the upper (red box) and lower (green box) regions of a cluster (Fe cluster), the variations shown in the image reveal the mixing and diffusion of elements and varying compositions present. The core region of the tooth is composed of a phosphorus-rich phase (blue). The purple-boxed area is a link between the iron-rich cluster and the phosphorus cluster (blue box).

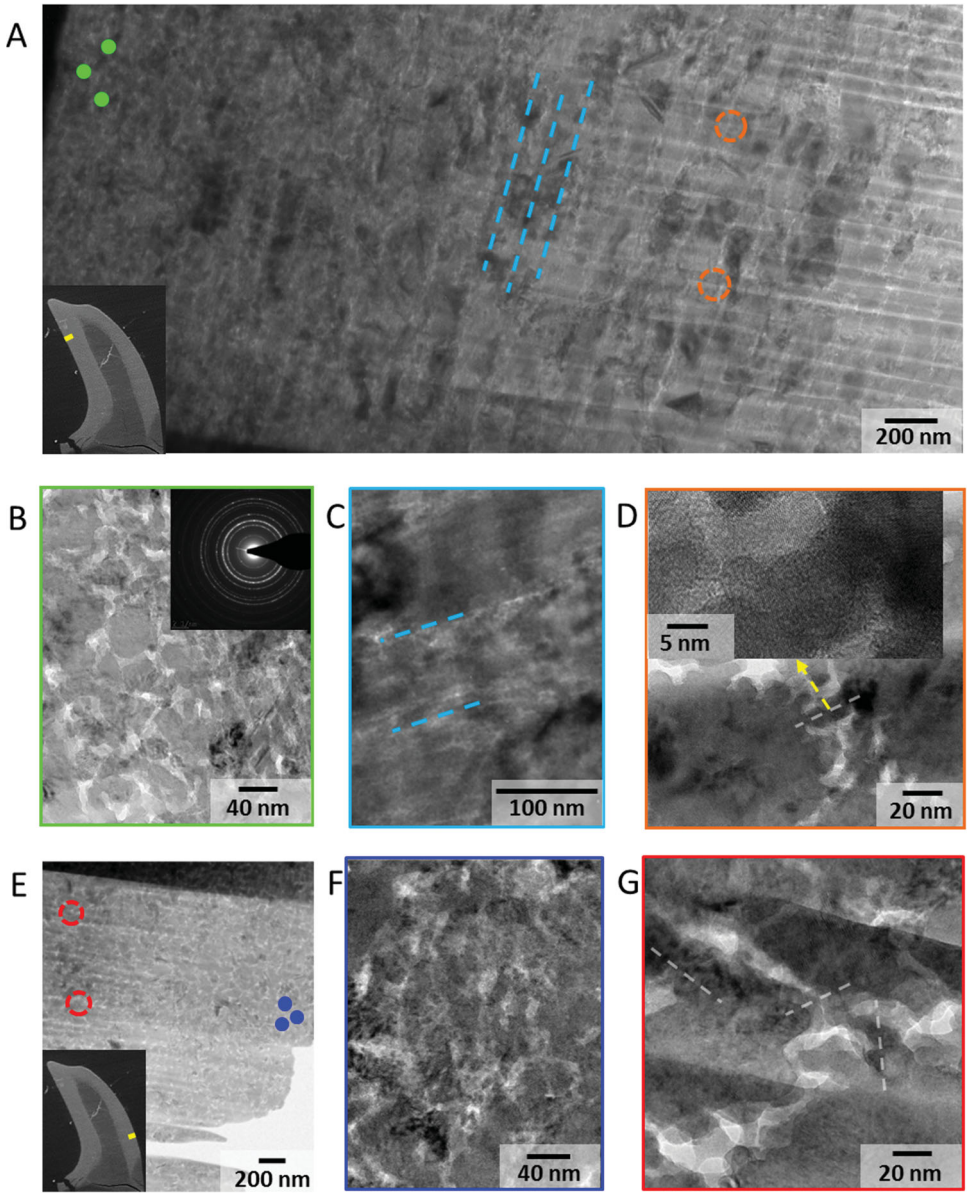

Figure 5. TEM analysis of FIB-sections from the leading and trailing edges of the tooth surface. A) Overview of the leading edge, showing the particulate layer at the outer edge of the tooth, transitioning to nanorods that rotate 90° until they are oriented parallel to the tooth surface. Inset: SEM image of a longitudinally polished section of tooth highlighting (in yellow) the region where the FIB section was obtained; B) Details of particulate outer layer, with selected area diffraction confirming the magnetite phase; C) Region where the long axis of nanorods are perpendicularly aligned with the tooth surface and rotate 90° to yield D) nanorods which are parallel to the tooth surface (observed here in cross-section, perpendicular to the field of view). Dashed white line and inset highlights mineral bridges connecting adjacent rods; E) Overview of the trailing edge, showing the particulate layer at the outer edge of the tooth abruptly transitioning to nanorods, which are parallel to the tooth surface. Inset: SEM image of a longitudinally polished section of tooth highlighting (in yellow) the region where the FIB section was obtained; F) Details of the dense nanoparticulate outer layer at the trailing edge, that transitions to G) nanorods, which are parallel to the tooth surface (mineral bridges shown by dashed white lines).

3. Modeling

Details of the geometry, ultrastructure and mechanical properties of the chiton tooth were employed to develop three-dimensional finite element models (FEM). A three-dimensional representation of the tooth was obtained using confocal fluorescence microscopy and subsequently digitized to obtain the CAD geometry (**Figure 7**A). The model was divided into four mechanically distinct regions. Each region is modeled with a linear elastic model with different values of Young's modulus obtained directly from the nanoindentation experiments: i) the tooth base (primarily consisting of alpha-chitin) (E = 7 GPa), ii) an iron phosphate core region (E = 35 GPa), iii) the leading edge (E = 130 GPa), and iv) the trailing edge of the magnetite shell (E = 105 GPa). A 0.1 N point force was applied at the tip of the tooth to simulate the working condition of the rasping of

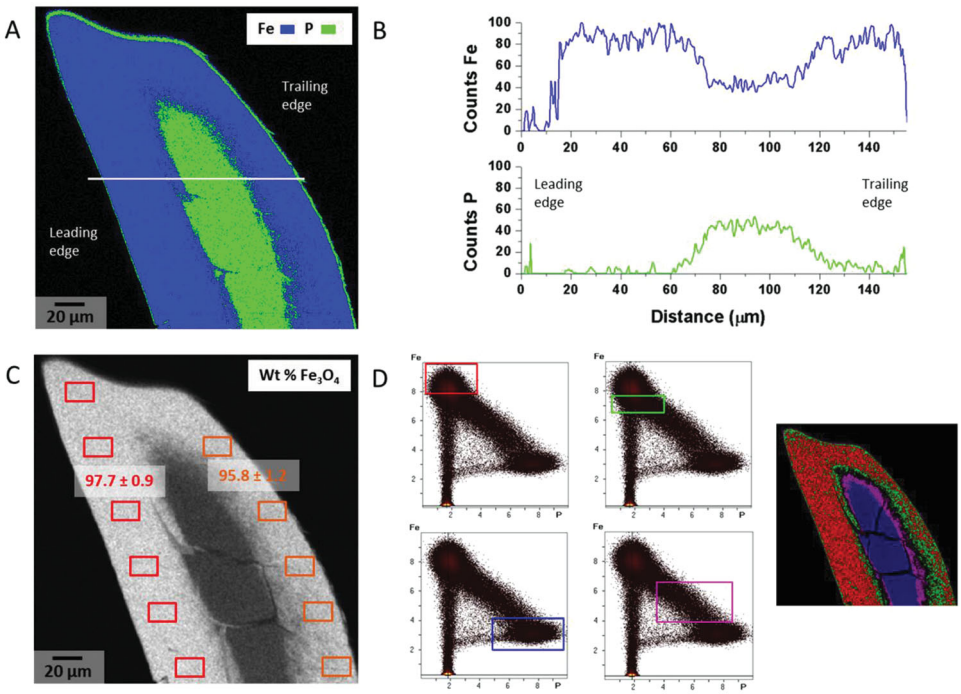

Figure 6. X-ray mapping (XRM and EDS) analysis results from a longitudinal section of the middle cusp from a fully mineralized tooth. A) False-colored map of iron (blue) and phosphorus (green) concentrations; B) Iron (blue) and phosphorus (green) concentrations as a function of tooth position, following the white line marked in A; C) BSE micrograph from which quantitation of magnetite (wt%) was calculated (based on averages of boxed regions on the leading and trailing edges); D) False-colored map of regions of unique concentration in the tooth obtained through analysis of scatter diagrams. Red- high concentrations of iron oxide; green- lower concentrations of iron oxide; blue- combination of iron and phosphorus-rich region; purple- combination of iron and phosphorus.

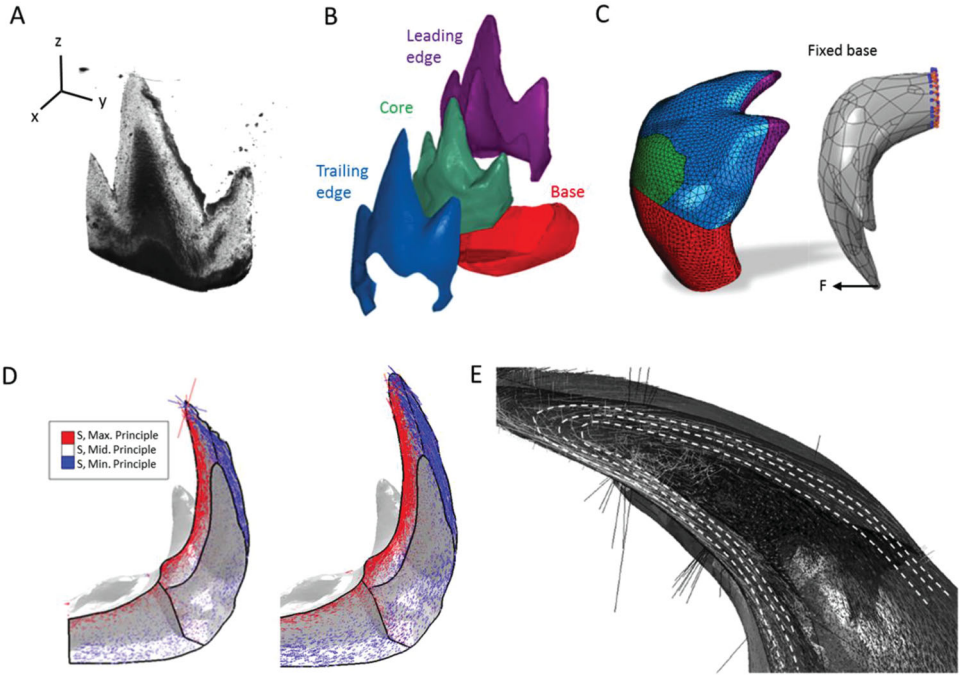

Figure 7. Finite element models of a fully mineralized tooth. A) Digitization of tooth geometry; B) The four individual components used to create the model and the association of each part into the full model; C) Mesh and boundary conditions; D) Direction of tensile (red) and compressive (blue) stresses in a worn (left) and fresh (right) tooth; E) Rotation in the direction of stresses at the transition zone between the leading and trailing edges above the core.

radular teeth. The four parts and their associations are shown in Figure 7B. The mesh and boundary conditions for the model are presented in Figure 7C.

The stress distribution in the tooth during a rasping event was revealed by the finite element model. In particular, Figure 7D shows the distribution of the principal stresses inside the tooth. The maximum tensile stresses (Figure 7D, red) are mainly distributed along the leading edge of the tooth and are parallel to the surface of the leading edge. On the other hand, the maximum compressive stresses (Figure 7D, blue) are concentrated along the trailing edge and are parallel to the surface of the trailing edge. The lines connecting the principal directions form the tensile and compressive trajectories. These principal directions are not altered by the gradual wearing of the tooth (Figure 7D). At the transition zone between the leading and trailing edges, the direction of the stresses rotates gradually as shown by the dashed lines in Figure 7E. This rotation of stresses is aligned with the rotation of rods observed in the transition zone above the core region (Figure 2D). Strain maps are presented in Figure S3 (Supporting Information).

At the microscale, a micromechanical model of uniform hexagonal rods that incorporates an inelastic model for the individual rods and a cohesive model that mimics the organic material was developed under a continuum finite element framework. As a rod diameter distribution has been identified, hexagonal rods of 150 nm and 250 nm were modeled (**Figure 8**A,B) with the elastic-plastic properties of single crystal magnetite. The yield stress of single crystal magnetite (σ_{yield} = 3.5 GPa) was obtained with the contact formulation presented by Johnson[22] and the hardening parameter was obtained by comparing the load versus displacement curves of computational models with experimental nanoindentation data of monolithic magnetite performed by Chicot et al.[23] Since it was shown that the mechanical properties of pure magnetite do not depend on crystallographic orientation, the model considers homogenous and isotropic elastic-plastic properties in the rod-like microstructure of the tooth. The interface between the rods is modeled with a cohesive zone model with a bilinear traction-separation law. The interface between the rods is modeled with a cohesive zone model with a bilinear traction-separation law.[24] The traction takes into account a high initial strength T_{max} = 1.5 GPa) to mimic the nanoscale features that prevent initial decohesion (e.g., mineral bridges and nanoasperities). The maximum displacement of the traction-separation law is defined as 200 nm, which is similar to values used for the organic material between nacre tablets.[25] As such, the fracture energy or work of separation is defined as G_c = 150 J m^{-2}. A cube corner indenter geometry was modeled as a rigid frictionless surface. Indentation curves show that despite the difference observed in the experimental data, the FEM indicates that at a penetration of ≈160 nm the total energy volume dissipated at the interfaces of the smaller rods (E_{dis} = 0.1225 nJ) is greater

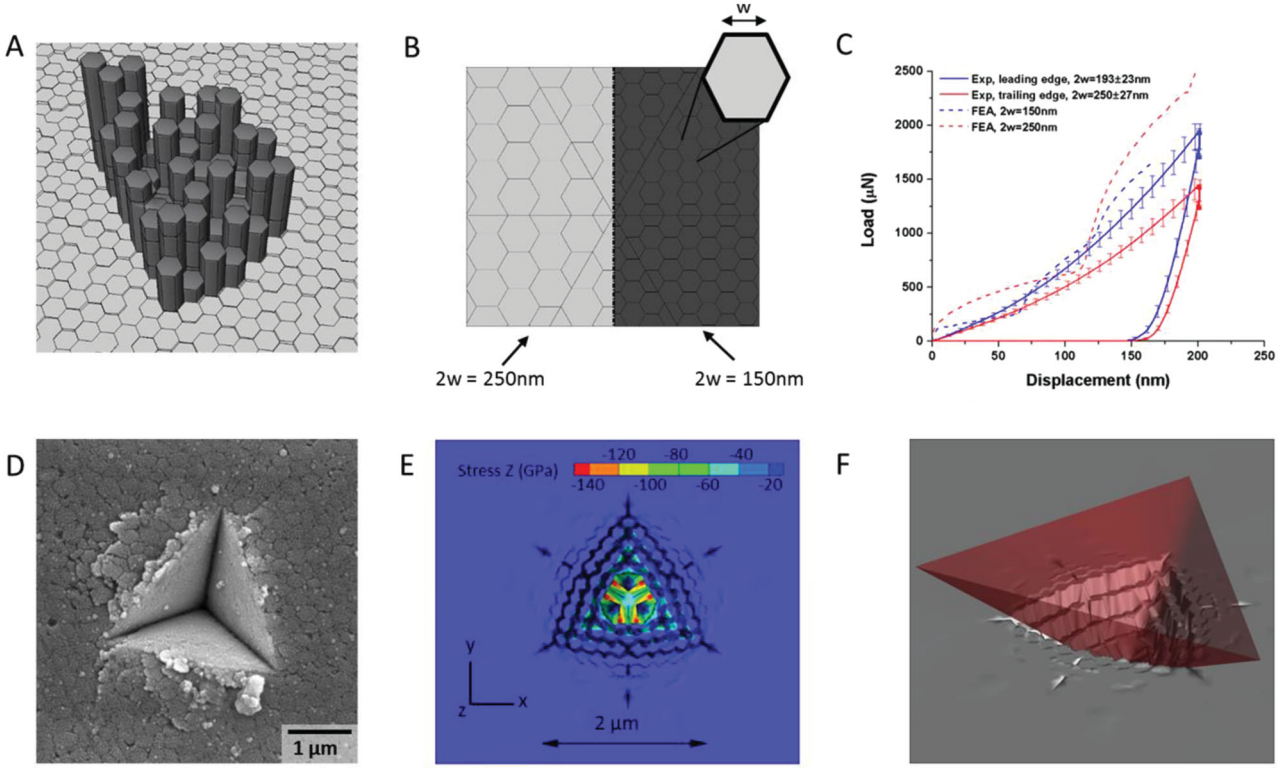

Figure 8. A) Pile up of staggered hexagonal rods idealized for illustration purposes to show the ultrastructure of the tooth; B) Rod cross sections assumed in the FEM for the trailing edge (250 nm) and leading edge (150 nm); C) Indentation data of experimental curves at the leading and trailing edge compared with the elastic-plastic FEM; D) Indentation mark at the leading edge of the tooth with rods aligned orthogonal to the surface; E) Comparison of stress contours in the same direction of indentation for an elastic model at maximum penetration (≈700 nm) showing material removal and crack propagation; F) Cube corner indenter placed above the model showing material removal and small radial cracks.

than those with a larger rod cross section (E_{dis} = 0.0062 nJ) (Figure 8C).

High-load nanoindentation was used to produce cracks in a latitudinal polished section (Figure 8D). Following indentation, the sample was sonicated in acetone to remove debris along with a surface layer of organic, revealing the mineralized rod structure. SEM imaging of this sample highlights that cracks do not progress radially from the corner of the indent, as is observed in monolithic materials,[26] but rather propagate around and between the mineralized rods in the organic-rich regions of the tooth (Figure 8D). The patterns of crack propagation are consistent with model results (Figure 8E), where small radial cracks of the size of an element are observed in the edges and material removal is shown surrounding the planes of the sharp indenter (Figure 8F).

4. Discussion

Engineering structures utilized in abrasive applications require constituent materials harder than the surfaces they contact.[22,23] Although hardness is a necessary factor in wear resistance, toughness is critical to maintaining longevity. Unfortunately, hardness and toughness generally have an inverse relationship.[27,28] Natural materials, however, utilize complex structures and a combination of inorganic and organic phases to achieve high hardness and toughness, a feature exemplified in the chiton tooth. While the tooth must be harder than the rocky substrate to abrade it and to resist wear, it must also be tough, as large stresses and intermittent impact forces are imposed during the grinding process. Through ultrastructural analysis and finite element modeling of the stresses imparted on chiton teeth during rasping, we observe how the organism has evolved features at the global and local scales to mitigate damage.

4.1. Bulk Features (Curvature, Core–Shell, and Deliberate Anisotropy)

Previous finite element simulations have shown that the curvature of the tooth leads to a redistribution of stresses to the base of the tooth, with the elimination of curvature resulting in stress concentrations at the tip of the tooth, where the structure is weak.[16] The hardness of the shell stems from mineralization by the hardest reported biomineral, magnetite.[6] In contrast, the soft core consists of an amorphous/nanocrystalline iron phosphate with a large fraction of organic.[5] This hard shell and soft core leads to crack deflection at the core–shell interface.[6,10] When a crack approaches an interface, it is propagated through, deflected, or arrested, depending on the relative stiffness of the materials on either side of the interface.[29–32] With a large modulus mismatch between the shell and core of the chiton tooth, crack deflection occurs (Figure 3H). This toughening mechanism has been reported in other biological composites, where deflection of cracks at an interface prevent catastrophic failure of the structure during repetitive loading.[30] Following cracking, a portion of the magnetite shell remains attached to the core (Figure 3H). This is consistent with previous studies, which have shown that the core–shell interface is rough, with interlocking between the two phases.[7] This interconnected interface results in tortuous paths for crack propagation, leading to significant energy dissipation. The graded nature of the interface between the core and shell can be seen in modulus and hardness maps (Figure 3) as well as elemental distribution maps (Figure 6).

The magnetite shell of the chiton tooth consists of mineralized rods aligned parallel to the tooth surface. This architecture is reminiscent of a fiber reinforced composite, a design which is inherently anisotropic, with high strength along the long axis of the fibers.[33] In the chiton tooth, as revealed by finite element simulations, the long axis of the mineralized rods is oriented in the direction of principle stresses at all stages of wear, providing increased strength (see Figure 2A, 7D, E). Additionally, there are differences in the loading as well as the architectures of the rods between the leading and trailing edges of the tooth. The three-dimensional finite element analysis, which is in agreement with previous work in 2D,[16] reveals a concentration of tensile stresses at the leading edge and compressive stresses at the trailing edge.

SEM analysis (Figure 4) reveals that rods on the leading edge of the tooth have a smaller diameter than those on the trailing edge (193 ± 23 nm vs 250 ± 27 nm). While rod diameter varies with tooth size as well as location, the trend of smaller diameter rods on the leading edge is consistent with previous observations.[8] In fiber reinforced composites, smaller diameter fibers are preferred for tensile loading[33] as they have fewer flaws, making them less brittle and therefore stronger in tension.[33,34] Thin fibers also have more flexibility, providing resistance to fracture during bending.[33] While unidirectional fibers perform well in tension, they are generally poor in compression. Composite longitudinal compressive strength, however, has been shown to correlate positively with fiber diameter.[34,35] These factors indicate that the larger diameter rods observed on the trailing edge of the tooth are optimized to withstand the compressive loading concentrated in this region. Finally, finite element simulations reveal a rotation of principle stresses at the transition zone between the leading and the trailing edges. These stresses are again parallel to the long axis of the rods, as shown in the rotation of rods around the core of the tooth (Figure 2D,F).

While the bulk of the rods in the chiton tooth are oriented parallel to the tooth surface, a rapid rotation of rods is observed in the first ≈5 μm of the leading edge (Figure 4A). This rotation acts as an initial line of defense against crack propagation. Multiple rod directions serve to hinder the propagation of microcracks, as cracks propagating along a rod in one direction are redirected when they reach a rod oriented in a different direction.[16,36,37] In *C. Stelleri*, the maximum stresses in the tooth are oriented parallel to the tooth surface. A crack initiating or propagating along the direction of principle stress would thus see the fibers at the edge of the tooth in a transverse orientation. Studies on fiber-reinforced composites have shown that initiation toughness increases by 26% when the crack propagation direction is transverse to the fibers (rather than parallel to them), and that fracture toughness increases with a rotation in fiber orientation angle.[38] As shown in Figure 3G, cracks are arrested at the outer region of the leading edge (≈4.4 μm into

the tooth), where rod rotation occurs, and are prevented from propagating into the bulk of the tooth. Preceding rod rotation on the leading edge of the tooth is a layer of magnetite particles. These particles, also found at the trailing edge, provide a barrier to material loss in early stages of tooth use, and are reminiscent of cellular structures formed at the surface of bulk materials where accommodation of large sliding strains is required.[39]

4.2. Local Features (Chemical and Nanostructural)

Nanoindentation maps (Figure 3) corroborate results from previous investigations,[6,16] highlighting the difference in hardness between the leading and trailing edges of the tooth, a design which results in a self-sharpening condition.[16] Variation in values at the trailing edge in latitudinal vs. longitudinal sections are assumed to arise because of rod orientation, with larger quantities of organic exposed along the long axis of the rods. Quantitative EDS analysis and the X-ray mapping results reveal that the hardness gradient in the tooth stems from a difference in the concentration of magnetite at the leading and trailing edges (Figure 6C). Furthermore, the modulus and hardness maps in Figure 3 reveal a trend in changes at the interfacial area between the core and the outer iron oxide shell that corresponds to the phase map in Figure 6D (light blue region of hardness and modulus). While variations in the degree of mineralization play a key role in the performance of the chiton tooth, the organic phase is equally important.

As observed in TEM (Figure 5C,D,G), and SEM (see Figure S4, Supporting Information), organic surrounds each mineralized rod.[6,37,40] Additionally, the organic fibers that template mineralization (Figure 2H) survive the mineralization process, resulting in organic within the rods.[7] The incorporation of organic in the chiton tooth influences mechanical properties at multiple length scales. From a bulk perspective, the presence of organic in the chiton tooth results in a reduction in the modulus of the material when compared to that of geologic magnetite.[6,10] For loading under blunt contact, a high ratio of hardness to modulus (H^3/E^2) is associated with an increase in abrasion resistance.[6,10,14] With its unique hardness to modulus ratio, the chiton tooth outperforms geologic magnetite in terms of abrasion resistance.[6,10] Incorporation of organic into the tooth also influences crack propagation. Through high-load nanoindentation, cracks were introduced into a latitudinal section of a chiton tooth (Figure 8D). Examination of the sample following indentation revealed that cracks propagate around the mineralized rods through the organic. This creates a tortuous crack pathway at the nanoscale, as corroborated in the micromechanical model, where the intricate microstructural alignment impedes crack propagation in the bulk, localizing the damage in the area surrounding the sharp geometry of the cube corner tip. At early stages of tooth mineralization, large multifaceted magnetite crystals are observed forming along organic fibers (Figure 2H). A crack deviating from the organic phase into a mineralized rod will thus encounter another toughening mechanism, in the form of additional interfaces induced from crystal faceting (Figure 2G). A crack traveling along the boundary between two adjacent magnetite crystals will be redirected along the contours of the crystal surface, resulting in energy dissipation.

TEM investigations have revealed additional toughening mechanisms at the nanoscale; specifically, the presence of surface asperities and mineral bridges. TEM results (Figure 5) show that the magnetite rods in the chiton tooth are formed from aggregated crystallites with no preferred orientation.[6,40] While the centers of these rods consist of larger crystallites, the perimeter is composed of a smaller (≈5 nm) nanoparticulate layer (see Figure S4, Supporting Information). These nanoparticles can be viewed as nanoasperities, creating peaks and valleys at the outer edges of the rods. Figure 5D demonstrates the interlocking design of these asperities, with peaks on one rod aligning with valleys in the adjacent rod. A similar architecture has been reported in nacre, providing resistance against interfacial sliding[41] and lateral expansion, which in turn leads to competing failure mechanisms that maximize energy dissipation.[42,43] The nanorods in the shell of the chiton tooth display another similarity to nacre, in the form of mineral bridges that connect adjacent magnetite rods (Figure 5D,G). These mineral bridges provide strength to the organic interface between rods and a barrier to crack propagation, leading to delamination resistance.[25] Additionally, crack deflection occurs at mineral bridges, further enhancing toughness.[44]

As showcased in this work, the chiton tooth combines features over multiple levels of hierarchy, resulting in an abrasion resistant structure. In the organism, tooth formation occurs continuously, and in-use teeth are discarded and replaced every 12–48 h in a growth-mediated process.[12,16,45] Despite this frequent replacement, radular teeth maintain the ability to abrade rock throughout their lifetime, representing a model system for advanced tooling materials. As a biological structure, the constituent materials that compose the tooth are limited to those available to the organism. The architecture of the tooth, however, lends remarkable toughness to the structure, and has adapted to withstand wear. Tooling materials inspired by the chiton tooth can utilize these architectural designs, along with high-performance materials, to eliminate the need to regularly replace components. For example, tungsten carbide-cobalt composites are a commonly used tooling material. The metallic matrix in these materials lends toughness to the composite, while the carbide phase results in high hardness and thus abrasion resistance.[27,28,46] Carbide particle size has been shown to influence abrasion resistance, with smaller grains leading to an increase in hardness, and an even greater increase in abrasion resistance.[28,46] Taking inspiration from the chiton tooth, a rod-like arrangement of carbide, aligned along the direction of principle stress, could provide further benefit.

The downside to carbide composites, however, is that are that they are expensive to process. A more economical route to the fabrication of abrasion resistant materials may lie in the use of bio-inspired synthesis methods to manufacture materials with controlled microstructures at ambient temperature. Biomineralizing organisms offer an environmentally friendly and low energy approach to the synthesis of these hierarchically assembled composites with controlled features.[8] Such an approach could also lend itself to the fabrication of biocompatible materials, a critical aspect for medical implants.

5. Conclusions

The design of abrasion resistant materials is a difficult task, as abrasion resistance is not an intrinsic material property, but dependent on a range of factors.[1–3] Rather than taking a trial and error approach to material design, however, engineers can draw inspiration from natural composites, which have evolved over millions of years. The chiton radular tooth is a complex hierarchically arranged composite, optimized to resist abrasive wear. Features of the tooth from the nano- to macroscale provide strength, abrasion resistance and toughness. The curvature of the tooth leads to a redistribution of stress concentrations away from the fragile tooth tip. A core–shell structure leads to crack deflection at the interface, preventing catastrophic failure. Rod orientation and diameter at various positions within the tooth provide strength optimized for specific loading conditions. Selective mineralization leads to a hardness gradient between the leading and trailing edges of the tooth, resulting in a self-sharpening condition, while incorporation of an organic phase results in a complex pattern of crack propagation. At the nanoscale, surface nanoasperities provide resistance to interfacial sliding between nanorods, and mineral bridges increase toughness. These factors, as well as bio-inspired synthetic routes gleaned from biominerals, can provide insights into the design and fabrication of abrasion resistant materials for applications such as tooling and machining.

6. Experimental Section

Research Specimens: Live specimens of *Cryptochiton stelleri* were obtained from a commercial supplier (Monterey Abalone Company, USA). Collection of *Cryptochiton stelleri* is permitted by the Department of Fish and Game, as well as the California Natural Resources Agency. Specimens were collected in the Eastern Pacific Ocean (off the coast of Monterey, California) and shipped overnight, packed in ice. Animals were dissected upon arrival and radula were removed. Intact radula were cleaned with DI water and then serially dehydrated to 100% ethanol immediately following dissection. Radula from several *Cryptochiton stelleri* were examined in this work, with animals ranging from 115–210 mm in length. While the tooth size scales with the size of the animal, the general shape and properties of the teeth remained consistent. As the fully mineralized teeth were the focus of this work, all teeth studied came from the first 10 rows of the anterior end of the radula. For embedding and polished sections, multiple teeth, still attached to the radular membrane, were cut from the radula using a razor blade. For fractured sections, individual teeth, still attached to the basal stock, were removed from the radula using non-magnetic fine-tipped tweezers.

Scanning Electron Microscopy: Individual dehydrated teeth were fractured using a hardened steel micro-knife (Precision Cutting Set, Ted Pella, USA). To prepare a fracture, the stock of the tooth was held with tweezers. After fracture, the stock, which is primarily organic, was removed. Samples were subsequently rinsed in ethanol to remove debris. Fractured samples were then placed onto carbon tape coated aluminum pin mounts. In some cases, specimens were subjected to additional sample preparation steps (see below). To remove organic, selected fractured samples were placed in an aqueous solution of 5% sodium hypochlorite for 8 hours. Following this treatment, an active wash in a fresh sodium hypochlorite solution was performed, followed by an active wash in deionized (DI) water and 3 consecutive DI washes of 10 minutes each on a shaker table. After washing, samples were mounted with carbon tape to aluminum pin mounts. Mounted samples were sputter coated with a thin layer of platinum and palladium to increase conductivity, and imaged using a scanning electron microscope (XL30-FEG, Philips, USA) at an accelerating voltage of 10 kV. For phase-contrast imaging, a backscatter electron detector was used, and the accelerating voltage was increased to 20 kV.

Transmission Electron Microscopy: To investigate the nanostructure at the surface of the tooth, a mature tooth was cut from an intact radula with a razorblade and fixed with gluteraldehyde (2.5%) in HEPES buffer (0.2 M, pH = 7.2) for 2 h. The sample was then serially dehydrated to 100% ethanol, embedded in resin (Spurr's low viscosity embedding kit, Sigma-Aldrich, USA) and cured for 24 h at 60 °C. The resin block was then sectioned with a diamond saw and polished in the longitudinal direction of the tooth with 1200 grit silicon carbide paper, followed by polishing with diamond lapping films down to 0.25 μm. Continued polishing yielded a longitudinal section of the middle cusp of the mature tooth. 100 nm thin sections from both the leading and trailing edge were milled from the longitudinal polished section with a Focused Ion Beam (FIB, Leo Gemini, 1540XB) and imaged using TEM (FEI-PHILIPS CM300) at 300 kV accelerating voltage.

Nanoindentation: Nanoindentation maps were performed on polished cross-sections of mature chiton teeth in both latitudinal and longitudinal directions. Indents were performed under ambient temperature using a nanomechanical testing system (TI 950 Triboindenter, Hysitron, USA). In preparation for testing, teeth that had been dehydrated in ethanol were serially embedded in epoxy (Spurr's low viscosity embedding kit, Sigma-Aldrich, USA). The resin block was then polished flat to reveal the plane of interest using a tripod polisher on 1200 grit silicon carbide paper. Additional polishing was then performed using diamond abrasive down to a 0.1 μm grit size. Because of the hardness of the teeth, polishing to lower grit sizes resulted in the erosion of the tooth core, and the epoxy around the tooth, leading to inaccurate indentation results. With flat polished sections prepared, displacement controlled indents were performed to a depth of 200 nm using a diamond cube corner indenter tip. Indents were performed in a grid with a spacing of 6 μm × 6 μm. The displacement function consisted of a 5 s loading step, a 2 s hold, and a 5 s unloading step. Hardness and elastic modulus were calculated using the Oliver and Pharr method.[47] Spatial maps of mechanical properties were produced using the XY position. Reduced modulus and indentation hardness were calculated from a mesh of MxN indents using the SCATTER function in MATLAB (MathWorks Natick, MA). High-load nanoindentation was performed to initiate cracking and observe fracture behavior. A latitudinal section was polished from an embedded radular tooth. Load-controlled indentation at was performed to a maximum load of 20 mN using a cube-corner tip, resulting in an indentation depth of just over 1000 nm. After indentation, the sample was sonicated in an acetone bath for 2 minutes to remove debris and surface organic.

Energy Dispersive Spectroscopy and X-Ray Mapping: Standardless quantitative elemental analysis was performed using JEOL 8600 EM Probe with a Moran Scientific Microanalysis system operated at 20 kV with a Kevex EDS detector. A software package called "Chemical Imaging" within the Moran Scientific system was used to post process the X-ray maps.[20,21,48] X-ray maps were collected at 512 × 512 pixel at 200 ms per point.

Confocal Fluorescence Microscopy: The shape of the tooth was reconstructed by confocal microscopy at the Purdue University Multi-Scale Imaging Center of the Bindley Bioscience Center. A single tooth, connected to a small portion of the stalk, was removed manually from the anterior-most region of a radula following dehydration. The tooth was air dried and then immersed in the mixture of oil and fluorescent dye (DiI) between two thin glass slices. The prepared "sandwich" was examined from each side under confocal microscopy with a 10× objective lens and 5 μm steps to obtain surface information. ImageJ, Amira5.3.0 and Catia v5 were used to combine the front and back surface data to generate the geometry of a full tooth.

Finite Element Analysis: Three dimensional finite element models were created to observe loading conditions in the tooth during use. The model from Catia obtained from the confocal fluorescence microscope was then imported to Abaqus and separated into four mechanically distinct

parts (base, core, leading edge, trailing edge). The Poisson's ratio for each part was assumed to be 0.3 and the elastic modulus was input from experimental nanoindentation values. The tooth model was fully meshed with 3D 4-node linear tetrahedrons, and the base of the tooth was set as fixed. Non-linear effects were excluded. The micro-mechanical model of 1/6 of the domain considers 6 node cohesive interface elements with normal and transversal traction in which material degradation occurs while reaching a maximum strength.[24] The nonlinear approach was implemented as a user subroutine in FEAP.[49] The stiff rods were modeled with a generalized plasticity law[50] of constants $\beta = 31.5$ GPa and R = 3 GPa.

Supporting Information

Supporting Information is available from the Wiley Online Library or from the author.

Acknowledgements

This work was supported in part by AFOSR: FA9550–12–1–0249 and ARO: W911NF-12–1–0257. The University of California, Riverside Central Facility for Advanced Microscopy and Microanalysis is acknowledged for the use of sample preparation and electron microscopy equipment. Dr. A. Taylor and the Bindley Bioscience Center at Purdue University are acknowledged for the imaging work using confocal fluorescence microscopy equipment. J. F. Rave Arango is thanked for contributions to the initial stages of tooth modeling. Simon Hager from the AMC Facility of UWS is acknowledged for assistance with collecting X-ray maps.

Received: April 5, 2014
Revised: May 27, 2014
Published online: August 11, 2014

[1] I. Hutchings, *Mater. Sci. Eng.* **1994**, *A184*, 185.
[2] D. Li, *Mater. Des.* **2000**, *21*, 551.
[3] K.-H. Z. Gahr, *Microstructure and wear of materials*, Elsevier, Amsterdam **1987.**
[4] S. Teoh, *Int. J. Fatigue* **2000**, *22*, 825.
[5] L. M. Gordon, D. Joester, *Nature* **2011**, *469*, 194.
[6] J. C. Weaver, Q. Wang, A. Miserez, A. Tantuccio, R. Stromberg, K. N. Bozhilov, P. Maxwell, R. Nay, S. T. Heier, E. DiMasi, D. Kisailus, *Mater. Today* **2010**, *13*, 42.
[7] M. Saunders, C. Kong, J. A. Shaw, P. L. CLode, *Microsc. Microanal.* **2011**, *17*, 220.
[8] Q. Wang, M. Nemoto, D. Li, J. C. Weaver, B. Weden, J. Stegemeier, K. N. Bozhilov, L. R. Wood, G. W. Milliron, C. S. Kim, E. DiMasi, D. Kisailus, *Adv. Funct. Mater.* **2013**, *23*, 2908.
[9] J. A. Shaw, D. J. Macey, L. R. Brooker, P. L. Clode, *Biol. Bull.* **2010**, *218*, 132.
[10] S. Amini, A. Miserez, *Acta Biomater.* **2013**, *9*, 7895.
[11] H. A. Lowenstam, *Geol. Soc. Am. Bull.* **1962**, *73*, 435.
[12] H. A. Lowenstam, S. Weiner, *On biomineralization*, Oxford University Press, Oxford **1989.**
[13] M. Nemoto, Q. Wang, D. Li, S. Pan, T. Matsunaga, D. Kisailus, *Proteomics* **2012**, *12*, 2890.
[14] H. C. Lichtenegger, H. Birkedal, J. H. Waite, *Heavy metals in the jaws of invertebrates*, (Eds: A. Sigel, H. Sigel, R. K. O. Sigel), John Wiley & Sons, West Sussex **2008**.
[15] L. R. Brooker, J. A. Shaw, *Advanced Topics in Biomineralization,* The chiton radula: A unique model for biomineralization studies, (Ed: J. Seto), Intech, Rijeka **2012**.
[16] P. Van der Wal, H. J. Giesen, J. J. Videler, *Mater. Sci. Eng. C* **2000**, *7*, 129.
[17] V. Imbeni, J. J. Kruzic, G. W. Marshall, S. J. Marshall, R. O. Ritchie, *Nat. Mater.* **2005**, *4*, 229.
[18] P. Zaslansky, R. Shahar, A. A. Friesem, S. Weiner, *Adv. Funct. Mater.* **2006**, *16*, 1925.
[19] H. Chai, J. J.-W. Lee, P. J. Constantino, P. W. Lucas, B. R. Lawn, *Proc. Natl. Acad. Sci.* **2009**, *106*, 18, 7289.
[20] K. Moran, R. Wuhrer, *Microchim. Acta* **2006**, *155*, 209.
[21] R. Wuhrer, K. Moran, *Microsc. Microanal.* **2013**, *19*, 828.
[22] K. Johnson, *J. Mech. Phys. Solids* **1970**, *18*, 115.
[23] D. Chicot, F. Roudet, V. Lepingle, G. Louis, *J. Mater. Res.* **2009**, *24*, 749.
[24] H. Espinosa, P. Zavattieri, *Mech. Mater.* **2003**, *35*, 333.
[25] F. Barthelat, H. Tang, P. Zavattierti, C.-M. Li, H. Espinosa, *J. Mech. Phys. Solids* **2007**, *55*, 306.
[26] D. Harding, W. Oliver, G. Pharr, *MRS Proceedings* **1994**, *356*, 663.
[27] K. Jia, T. Fischer, *Wear* **1996**, *200*, 206.
[28] A. Lansdown, A. Price, *Materials to resist wear: A guide to their selection and use*, Pergamon Press, Oxford **1986**.
[29] M.-Y. He, J. W. Hutchinson, *Int. J. Solids Struct.* **1989**, *25*, 1053.
[30] J. C. Weaver, G. W. Milliron, A. Miserez, K. Evans-Lutterodt, S. Herrera, I. Gallana, W. J. Mershon, B. Swanson, P. Zavattieri, E. DiMasi, D. Kisailus, *Science* **2012**, *336*, 1275.
[31] P. Fratzl, H. S. Gupta, F. D. Fischer, O. Kolednik, *Adv. Mater.* **2007**, *19*, 2657.
[32] P. Murali, T. K. Bhandakkar, W. L. Cheah, M. H. Jhon, H. Gao, R. Ahluwalia, *Phys. Rev. E* **2011**, *84*, 01502.
[33] A. K. Kaw, *Mechanics of composite materials*, CRC Press, Boca Raton **2006**.
[34] S. Bazhenov, A. Kuperman, E. Zelenskii, A. Berlin, *Compos. Sci. Technol.* **1992**, *45*, 201.
[35] Y. L. Xu, K. L. Reifsnider, *J. Compos. Mater.* **1992**, *27*, 572.
[36] P. Van der Wal, *J. Ultrastruct. Mol. Struct. Res.* **1989**, *102*, 147.
[37] P. Van der Wal, *Structure and formation of the magnetite-bearing cap of polyplacophoran tricuspid radular teeth*, (Eds: R. B. Frankel, R. P. Blakemore), Plenum Press, New York **1991**.
[38] J. Andersons, M. Konig, *Compos. Sci. Technol.* **2004**, *64*, 2139.
[39] D. Rigney, W. Glaeser, *Wear* **1978**, *46*, 241.
[40] K. M. Towe, H. A. Lowenstam, *J. Ultrastruct. Res.* **1967**, *17*, 1.
[41] R. Wang, Z. Suo, A. Evans, N. Yao, I. Aksay, *J. Mater. Res.* **2005**, *16*, 2485.
[42] J. Rim, P. Zavattieri, A. Juster, H. Espinosa, *J. Mech. Behav. Biomed. Mater.* **2011**, *4*, 190.
[43] H. Espinosa, A. Juster, F. Latourte, D. Gregoire, O. Loh, P. Zavattieri, *Nat. Commun.* **2011**, *2*, 173.
[44] S. Fan, B. Yilong, *Acta Mech. Sin.* **2001**, *17*, 251.
[45] K. M. Towe, H. A. Lowenstam, M. H. Nesson, *Science* **1963**, *142*, 3588, 63.
[46] H. Liao, B. Normand, C. Coddet, *Surf. Coat. Technol.* **2000**, *124*, 235.
[47] W. Oliver, G. Pharr, *J. Mater. Res.* **2004**, *19*, 3.
[48] K. Moran, R. Wuhrer, *Microchim. Acta* **2006**, *155*, 59.
[49] O. Zienkiewicz, *The finite element method,* McGraw-Hill, London, New York **1977**.
[50] J. Lubliner, R. Taylor, F. Auricchio, *Int. J. Solids Struct.* **1993**, *30*, 3171.